An $FeNbO_4$-based oxide anode for a solid oxide fuel cell (SOFC)

Xiaojing Liu[a], Deti Xie[a], John T.S. Irvine[b], Jiupai Ni[a]* and Chengsheng Ni[a]*

a College of Resources and Environment, Southwest University, Chongqing, Beibei, 400715, China

b School of Chemistry, University of St Andrews, Fife, KY16 9ST, UK

Email: J.N. nijiupai@163.com; C.N. nichengsheg@swu.edu.cn; nichengsheg@163.com.

Abstract

The advantage of n-type semiconductor for an anode of solid oxide fuel cells (SOFCs) lies in its higher electronic conductivity in reducing atmosphere than in air. In this study, *n*-type $FeNbO_4$-based oxides that can be reduced at temperatures below 700 °C for a conductivity above 1 S cm^{-1} are explored as anode materials for a ceria-based SOFC utilizing liquefied-petroleum-gas (LPG) fuel apart from pure H_2. $Fe_{0.8}Nb_{1.2}O_4$ with 20 at.% Fe deficiency was founded in the sample sintered at 1250 °C. The structure stability of $FeNbO_4$ under reducing atmosphere can be improved by its solid solution with a less-reducible TiO_2 that also stabilizes the high-temperature α-PbO_2 type structure with mixed Fe^{3+} and Nb^{5+} cation. In particular, a full cell employing $Ti_{0.36}(Fe_{0.985}Nb_{1.015})_{0.84}O_4$, a stable and electrically conductive (1 S cm^{-1}) oxide in 5% H_2, as anode shows a powder density of 180 mW cm^{-2} at 700 °C if 0.5 wt.% Pd is impregnated to increase the electrocatalysis and the electric loss is mostly from the electrolyte. The oxide anode showed a degradation (20% during the 5 to 26 hours aging) and the carbon deposition is slight after 5-hour operation under an LPG fuel.

Introduction

Solid oxide fuel cells (SOFCs) are regarded as low-emission power generation devices

[1] and are not restrained by efficiency limitations applicable to heat engines (*i.e.* the Carnot cycle). The potential widespread use of SOFCs also depends on the availability of fuel[2]. Comparing to the low-temperature proton-exchange-membrane fuel cell (PEMFC), the advantage of an all-ceramic SOFC device could be the ability to use carbonaceous fuel, i.e. carbon monoxide, methane et al., other than pure H_2 fuel[3-6]. The fuel versatility of an SOFC increases the fuel availability since the infrastructure for carbonaceous fuel is mature, which will facilitate the commercialization of this technique and reduce the additional cost on H_2 storage and transport[2]. The conventional nickel-based anode catalyzing the oxidation of the H_2 fuel on GDC electrolyte is Ni(O)-GDC cermet and a high performance (e.g. 2 W cm^2 at 550 °C)[7] has been achieved via the optimization of the cathode materials and the thinning of the electrolyte[8]. However, the carbon deposition or coking process of the Ni under a carbonaceous fuel would prohibit the long-term operation for continuous power supply[9] and thus novel oxide perovskites, such as (La, Sr)(Cr, Mn)O_3, Sr_2MoMO_6 (M=Mg, Cr or Mn) and (La, Sr)TiO_3, has been developed for the operation under hydrocarbon fuels[10-20].

Generally, both *n*- and *p*-type semiconducting oxides can be used as the anode materials in an SOFC. $La_{0.75}Sr_{0.25}Cr_{0.5}Mn_{0.5}O_3$ is a paradigmatic *p*-type semiconducting oxide showing a decreased conductivity under reducing atmosphere of fuel than in air, while (La, Sr)TiO_3 is an *n*-type semiconductor showing superior stability and conductivity if is fully reduced[21] at elevated temperatures[22] (above 750 °C under H_2). However, an SOFC under the intense *in-situ* reduction at elevated temperature for anodes can possibly induce the reduction of the GDC electrolyte, causing the increase of electronic conduction and internal stress of the ceria-based electrolyte[23, 24]. A perovskite-type oxide $Sr_{0.2}Na_{0.8}Nb_{1-x}V_xO_3$ (x= 0.1-0.3) has been explored as low-temperature anode and a high-conductivity (300 S cm^{-1}) is achieved under mild reduction at 650 °C[25] as a result of the transition between V^{4+} and V^{3+}.[26] Moreover, although an oxide anode can inhibit the deposition of carbon, the poor catalytic ability for the oxidation of fuel needs to be improved [27, 28]. One strategy of improving the electrocatalysis could be the decoration

of metal catalyst (e.g. Pd, Ni, et al.) onto the oxide anode through infiltration or in-situ exsolution[26, 28-32].

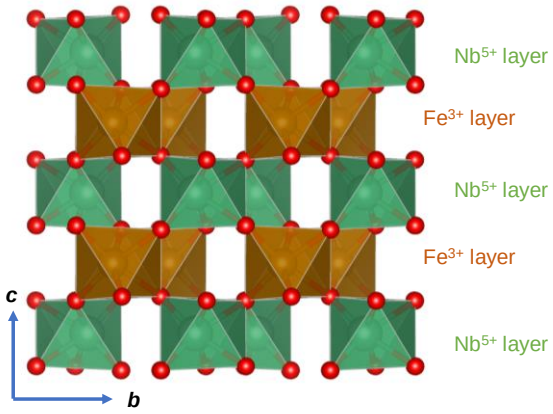

Figure 1. Crystal structure of a monoclinic wolframite $FeNbO_4$ with Fe^{3+} and Nb^{5+} ordering on either side of the *hcp* oxide-ion planes. The orthorhombic α-PbO_2 polymorph is quite similar but with a random Fe^{3+} and Nb^{5+} distribution.

$FeNbO_4$-based oxides with multiple phase transitions and was explored as oxide anodes that can be reduced below 700 °C.[33] Due to the charge difference of Fe^{3+} and Nb^{5+} cations, they reside on either side of a hexagonal-close-packed (*hcp*) oxide ions at low temperatures (graphically represented in Figure 1 and noted as wolframite) or distributed randomly on both sides of the *hcp* oxide ions at temperatures higher than 1085 °C (noted as α-PbO_2 type polymorph)[33-35]. The α-PbO_2 type $FeNbO_4$ can transform to a rutile-type with a linear cation arrangement on either side of the oxygen layer at temperature above 1380 °C[35]. At temperature below 800 °C, Nb^{5+} is generally stable under the reduction of H_2[36, 37] and the reduction of Fe^{3+} under reducing condition increases the fraction of Fe^{2+} in the structure and induces an *n*-type conduction[38], but the pathway of electronic defects is confined in the zig-zag Fe-O-Fe bonds that are separated by the Nb-O-Nb layers. The dimensionality of inorganic materials has been explored as it could cause dramatic effect on the charge carriers for light-harvesting materials[39, 40], but the similar observation on electronic materials is also interesting for the property and functional modification of an anode of an SOFC. The

random distribution of Fe^{3+} and Nb^{5+} cation in the α-PbO_2 structure could increase the percolation of Fe-O-Fe bonds, causing a three-dimensional electronic conduction path[41]. Moreover, for the practical use of an oxide anode in SOFC, the stability of the oxide under a reducing atmosphere is also important. The cation ordering in $FeNbO_4$ could also change the local oxygen-vacancy concentration when oxygen atoms were removed from lattice and thus the stability under a reducing atmosphere. The high temperature phase of $Fe_{1-\gamma/3}Nb_{1+\gamma/3}O_4$ ($0 \leqslant \gamma \leqslant 0.09$) and transition in cation ordering were studied via the quenching of the samples from 1250 °C directly to room temperature. Since the oxygen loss from the lattice can also be decreased by substituting Fe^{3+} with the less reducible ones, the solid solution between $Fe_{0.985}Nb_{1.015}O_4$ and TiO_2 is explored in this study to improve the stability of this material under a fuel condition. With a GDC electrolyte of 200 μm in thickness we obtained a performance around of 180 mW cm^{-2} at 700 °C with a $Ti_{0.36}(Fe_{0.985}Nb_{1.015})_{0.84}O_4$-based anode.

Experimental

Materials synthesis A solid-state method using Fe_2O_3 (Macklin, 99.9%), Nb_2O_5 (CIVI Chemicals, 99.99%), TiO_2 (Macklin, 99.9%) as precursors was employed to synthesize the bulk $Fe_{1-\gamma/3}Nb_{1+\gamma/3}O_4$ ($0 \leqslant \gamma \leqslant 0.60$) and $Ti_{2x}(Fe_{0.985}Nb_{1.015})_{1-x}O_4$ ($0.05 \leqslant x \leqslant 0.25$) solid solutions. In short, stoichiometric oxide precursors were weighed, mixed in an agate mortar for 30 minutes and pelletized before the firing at 1250 °C for $Fe_{1-\gamma/3}Nb_{1+\gamma/3}O_4$ ($0 \leqslant \gamma \leqslant 0.60$) and 1050 °C for $Ti_{2x}(Fe_{0.985}Nb_{1.015})_{1-x}O_4$. The ramp rate for a normal heating and cooling was 3 °C min^{-1} and the dwelling time was 5 hours. For the quenched samples of $Fe_{1-\gamma/3}Nb_{1+\gamma/3}O_4$ ($0 \leqslant \gamma \leqslant 0.09$, noted as $Fe_{1-\gamma/3}Nb_{1+\gamma/3}O_4$-Q), the sintered samples were reheated at 1220 °C for 30 minutes, taken out of the furnace directly and cooled in air.

$Ti_{0.36}(Fe_{0.985}Nb_{1.015})_{0.84}O_4$, noted as TFN-36, was selected as the candidate for an SOFC due to the acceptable conductivity and stability under a reducing atmosphere and the nanoparticles were synthesized via combustion method: the soluble precursors of $C_6H_{18}N_2O_8Ti$ (50% w/w aqueous solution, Alfa Aesar), niobium oxalate (Macklin, 98%) and

$La(NO_3)_3 \cdot 6H_2O$ (Macklin, 99%) were weighed and dissolved in deionized water. The solution was dried while stirring at 80 °C and then ignited at 350 °C to produce the raw powder that would be calcined at 970 °C for 5 hours for the nanoparticles. $Gd_{0.15}Ce_{0.85}O_{1.95}$ (GDC) powder for the electrolyte and $La_{0.6}Sr_{0.4}Co_{0.2}Fe_{0.8}O_{3-\delta}$ (LSCF) powder for cathode were synthesized at 900 °C for 5 hours using the respective nitrate precursors in a similar combustion process.

Materials characterization Bar-shaped samples (70% in density and 2mm x 2mm x 11mm in dimension) were used for the conductivity measurement while attached with four pieces of silver wire. The conductivity was recorded using a computer-controlled Keithley 2100 multi-meter during the heating in air and cooling under 5% H_2 balanced with argon (Ar-5% H_2). At 700 °C, an Ar-5% H_2 flow was introduced and isothermal conductivity was recorded for about 10 hours prior to the cooling process. X-ray diffractions (XRDs) of the powdered samples were recorded on a diffractometer with a graphite monochromator (Cu $K_{\alpha 1}$, λ=1.54056Å, XD-3, Persee, China). Rietveld fitting of the XRDs was performed to determine the cell parameters using a General Structure Analysis System (GSAS) software. Thermogravimetry analysis (TGA) were carried out on a thermal balance (Netzsch F3, Germany) under 25 mL min^{-1} Ar-5% H_2. The compatibility test was performed by calcining the mixed powder (1:1 by weight) of TFN-36 and GDC at 1000 °C for 4 hours, and then XRD of the mixture was obtained at room temperature to analyze the interaction between them.

Fuel cell assembly and testing GDC powder was pelletized and sintered at 1500 °C for 5 hours to obtain a dense electrolyte, and then its thickness was reduced to 200 μm by polishing with sandpaper. The slurry for the electrodes was prepared by mixing the powder (1:1 by weight) with a vehicle containing 5 wt.% polyvinylpyrrolidone and 95 wt.% terpineol (Macklin, mixed polymorphs, 99.9%). For the preparation of a full cell, the painted green films of the mixed GDC and LSCF (4:6 in weight ratio) cathode and TFN-36 anode on either side of the electrolyte was dried at 80 °C in air and then calcined at 1000 °C for 4 hours. The area of the two electrodes was 0.4 cm^2. The fuel cell was mounted on an

alumina tube using a ceramic bond and electrochemical performance was tested using humidified H_2 or liquefied petroleum gas (LPG, 5-6 vol.% H_2, 10 vol.% CH_4, 5 vol.% C_2H_6, 10 vol.% C_3H_6, 3 vol.% C_2H_4, 3 vol.% H_2O, 10 vol.% C5-C6 alkane and balance C_3H_8 and C_4H_{10}; S impurity: 40 mg m^{-3}) as fuel[42, 43]. The flow rate of fuel was 25 mL min^{-1} and the cathode was exposed in static air. In order to enhance the electrocatalytic performance, 0.1 M $PdCl_2$ solution was impregnated onto the anode side[26] and dried at 500 °C for 30 minutes. The Pd loading was estimated to be 0.5 wt.% of the electrode by the weight change.

Electrochemical measurements, including current-voltage (I-V) and current-power (I-P), were performed on a Zahner Pro workstation (Zahner, Germany). Specifically, the electrochemical impedance spectroscopy (EIS) was procured in the frequency range between 1MHz and 0.01 Hz using a sine voltage wave of 10 mV amplitude. X-ray photoelectron spectroscopy (XPS) was obtained with a Thermo ESCALAB 250Xi spectrophotometer using 150 W Al K_α radiation and for peak calibration adventitious C 1s was set at 284.9 eV. Scanning electron microscopy (SEM) of the samples was performed on ZEISS SUPRA 55 Field Emission Scanning Electron Microscope.

Results and discussions

Structure and cation non-stoichiometry of wolframite-type samples

The conductivity of $FeNbO_4$-based materials synthesized in air was attributed to the presence of Fe^{2+} during the firing process and the final product was found to be a solid solution between $Fe^{III}NbO_4$ and $Fe^{II}Nb_2O_6$ ($Fe_{0.33}Nb_{0.67}O_4$), where the Nb content could be higher than unity[44, 45]. The tolerance for Fe^{2+} in the structure was studied by synthesizing different oxides in the formula $(FeNbO_4)_{1-\gamma}(Fe_{2/3}Nb_{4/3}O_4)_\gamma$ or $Fe_{1-\gamma/3}Nb_{1+\gamma/3}O_4$ ($0 \leqslant \gamma \leqslant 0.60$), whose XRD patterns are shown in Figure 2a. Monophasic wolframite can be obtained by slow cooling (3-5 °C min^{-1}). The Rietveld fitting of the $FeNbO_4$ as an example is shown in Figure 2b and one can see that the crystal structure is monophasic and

monoclinic, with a symmetry of P2/c. The calculated tilting angle, β, is 90.18° as a result of the cation ordering of Fe^{3+} and Nb^{5+} that occupies either side of the *hcp* oxygen layer. The Fe^{2+} fraction in air is related to the composition and oxygen partial pressure of the synthetic condition. As the ionic size of Fe^{2+} (75 pm) is larger than that of Fe^{3+} (69 pm), the oxides showed a constant expansion in cell volume (Figure 2c) for the investigated stoichiometries and a linear plot can be obtained if γ is less than 1.1. When γ is greater than 1.2, the slope between γ and the cell parameters decreases in the *b* and *c* direction while *a* parameter starts to decrease. When the niobium content is higher, the transfer of Nb^{5+} in the $Fe^{2+/3+}$ layer cannot be excluded, since the high-level cation deficiency might cause instability in the structure. However, one can clearly see that the wolframite structure can tolerate high Fe-deficiency, and the solubility of $FeNb_2O_6$ in wolframite-type $FeNbO_4$ should be higher than 60% at 1250 °C.

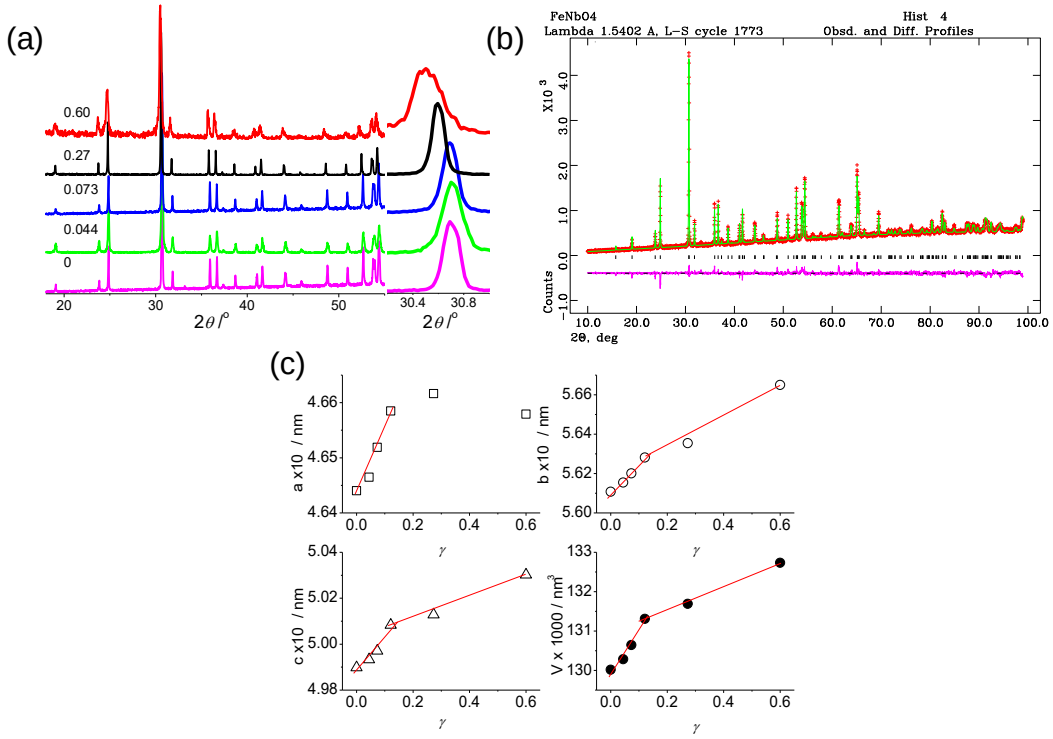

Figure 2. (a) XRDs of the wolframite-type $Fe_{1-\gamma/3}Nb_{1+\gamma/3}O_4$ ($0 \leqslant \gamma \leqslant 0.60$) and (b) Rietveld fitting of the XRD of a wolframite-type $FeNbO_4$: symmetry P2/c, χ^2 = 1.4, Rp=0.04 and wRp=0.06. (c) unit cell parameters at different γ values in term of *a*, *b*, *c* and cell volume,

V. The sample $Fe_{0.8}Nb_{1.2}O_4$ is synthesized at 1250 °C under an argon atmosphere while the others in the ambient air. The main peaks at around 30.7° (2θ) were magnified in (a) to highlight the peak shift as a result of cell parameter variation. The vertical ticks and the line at the bottom in (b) are the position of peaks and the difference between the fitted and measured data, respectively.

Effect of quenching on the structure and properties

A high-temperature orthorhombic α-PbO_2 structure can be obtained at temperatures above 1085 °C after the randomization of Fe^{3+} and Nb^{5+} on the cation sites[35]. In order to maintain the high-temperature α-PbO_2 phase, the sample was quenched from 1220 °C and then cooled in the ambient air. The $FeNbO_4$ and $Fe_{0.985}Nb_{1.015}O_4$ samples preserve the α-PbO_2 phase while $Fe_{0.97}Nb_{1.03}O_4$ shows a wolframite structure according the room temperature XRDs (Figure 3a). The cell parameters (Table 1) of the quenched samples display an inverse trend against the slowly cooled ones since the cell volumes decreases with the niobium content, which could be related to the extent of cation disordering in the structure.

Table 1. Unit-cell parameters of the quenched samples

	Symmetry	*a* / Å	*b* / Å	*c* / Å	β / °	*V* / Å^3
$FeNbO_4$-Q	Pbcn	4.6554(3)	5.6278(3)	5.0075(3)	90	131.190(8)
$Fe_{0.985}Nb_{1.015}O_4$-Q	Pbcn	4.6530(3)	5.6203(3)	5.0035(3)	90	130.851(9)
$Fe_{0.97}Nb_{1.03}O_4$-Q	P2/c	4.6532(2)	5.6220(2)	5.0002(2)	90.217(4)	130.809(7)
$FeNbO_4$[a)]	P2/c	4.6440(4)	5.6107(5)	4.9898(5)	90.180(6)	130.016(3)
[a)] The slowly cooled wolframite type oxide for comparison.						

Considering that the random distribution of $Fe^{2+/3+}$ in the α-PbO_2 type oxides could induce a 3-D Fe-O-Fe path for electronic conduction [41], oxide conductivities in air and

hydrogen were measured (Figure 3b). The quenched samples showed a higher conductivity in air than those of the unquenched ones: *e.g.* the conductivity of $FeNbO_4$ tested at 700 °C in air increased from 1.0 to 2.0 S cm^{-1} *via* the quenching process. The conductivity for all the samples were stable in air, indicating that the absorption of oxygen or phase transformation at 700 °C was minor. More importantly, the conductivity of the orthorhombic samples was more stable than the wolframite counterparts under Ar-5% H_2. The reduction under an Ar-5% H_2 induced an obvious increase in conductivity for those wolframite samples at the beginning, but little such increase was observed for the α-PbO_2 type oxides (i.e. $FeNbO_4$-Q and $Fe_{0.985}Nb_{1.015}O_4$-Q). For monoclinic $Fe_{0.97}Nb_{1.03}O_4$-Q, the conductivity data changed very little compared to the unquenched one. This result further indicated that phase change or cation ordering/disordering could be the main reason for the conductivity change in $FeNbO_4$-Q and $Fe_{0.985}Nb_{1.015}O_4$-Q. The initial increase of conductivity in air could possibly be related to the variation in oxygen content and fraction of Fe^{2+}, while the stable conductivity in the reducing atmosphere was resulted from the cation ordering in the structure. As the activation energy of the $Fe_{0.985}Nb_{1.015}O_4$ sample in air and in Ar-5% H_2 is around 0.39 eV and 0.25 eV (Figure 3c), respectively, which is much smaller than 1.0 eV and thus related to the enthalpy of migration of electronic defects[46]. Moreover, in a wolframite $FeNbO_4$, the bond angles of Fe-O-Fe is 99°, but it could change to 129° across the MO_2 (M=Fe or Nb) plane in an α-PbO_2 structure and the change in the bond angle would be related to the smaller activation energy of the later in both air and reducing atmosphere[47].

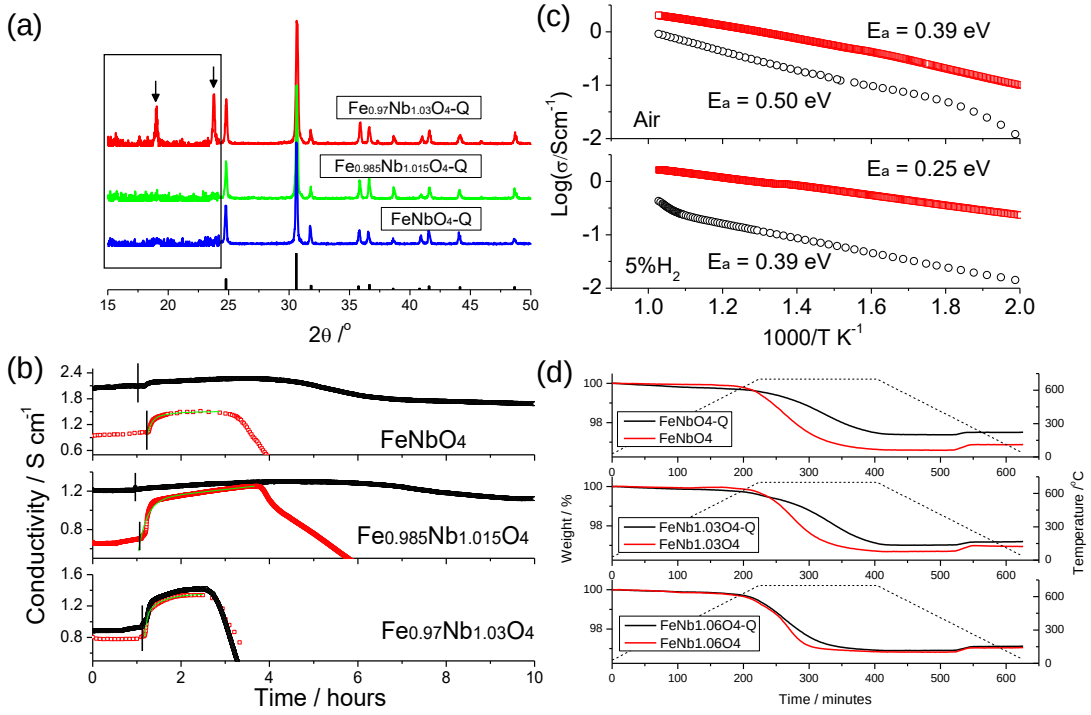

Figure 3 (a) XRDs of the quenched $Fe_{1-\gamma/3}Nb_{1+\gamma/3}O_4$ ($0 \leqslant \gamma \leqslant 0.09$) (the data in the rectangle box is magnified by 5 times to highlight peak for monoclinic phase); (b) Isothermal conductivity of $Fe_{1-\gamma/3}Nb_{1+\gamma/3}O_4$ ($0 \leqslant \gamma \leqslant 0.09$) at 700 °C sintered at 1250 °C with (black dots) and without (red dots) an additional quenching at 1220 °C; (c) Arrhenius plots of the quenched (red squares) and unquenched (black circles) $FeNbO_4$ sample during the heating in air and the cooling under Ar-5% H_2 after the reduction at 700 °C; (d) TGA of the quenched (black line) and unquenched (red line) samples. The arrows in (a) indicate the peaks for wolframite-type structure and the vertical lines at the bottom are the standard peaks for α-PbO_2. The vertical lines in (b) delimit the reduction process.

The structure stability of an anode under a reducing atmosphere is of critical importance because the undesired phase transition can cause stress or insulating phases on the electrolyte/electrode interface[26]. TGA of the quenched and unquenched samples shows that an α-PbO_2 phase in $FeNbO_4$ and $Fe_{0.985}Nb_{1.015}O_4$ retards the oxygen

loss at 700 °C under Ar-5% H_2, while the $Fe_{0.97}Nb_{1.03}O_4$ without the phase transition shows little variation in weight loss. The oxygen-loss rate in a bulk solid is related to the oxygen vacancies induced by the removal of oxygen in the superficial layer[48]. In a wolframite phase with $Fe^{2+/3+}$ cation on the same layer, the aggregation of oxygen vacancies destabilizes the structure, which is in accord with the faster weight loss under a reducing atmosphere. Moreover, as the weight loss is associated with the loss of oxygen bonding with Fe^{3+} cation, the Fe-O bond length is also very important. For example, the Fe-O bonds in a wolframite $FeNbO_4$ are 2.11 and 2.01 Å, while those in the α-PbO_2 counterpart are 2.12 and 1.92 Å. The shorter and stronger Fe-O bonds in the latter can also be related to the improved stability. The XRD patterns (Figure S1) of the $Fe_{0.985}Nb_{1.015}O_4$, or $Fe_{0.985}Nb_{1.015}O_4$-Q samples after TGA show that they decompose to mixed $FeNb_2O_6$ ($Fe_{0.33}Nb_{0.67}O_4$) and $FeNbO_{4-\delta}$ phases. As the tri-rutile $FeNb_2O_6$ was found to be insulating[49], the lower oxygen loss in the quenched samples is consistent with the smaller conductivity decrease after extended reduction.

Solid solution between $Fe_{0.985}Nb_{1.015}O_4$ and TiO_2

Although the α-PbO_2 phase retards the oxygen-loss rate of the oxides, $Fe_{1-\gamma/3}Nb_{1+\gamma/3}O_4$ (γ=0 and 0.045) samples are theoretically unstable under the reducing under 5% H_2 at 700 °C. Therefore, the incorporation of Ti^{4+} into the lattice is explored and the XRDs of the samples with the nominal formulae $Ti_{2x}(Fe_{0.985}Nb_{1.015})_{1-x}O_4$ ($0.05 \leqslant x \leqslant 0.25$) are shown in Figure 4a. The slightly higher concentration of Nb than Fe is designed for better phase purity. For the sample with x values of 0.05 and 0.11, one can still see some wolframite phases in the product, while for those samples with an x value of 0.18, an orthorhombic phase with randomly distributed cations is preserved even with the normal cooling rate at 3 °C min^{-1}. The low-temperature cation ordering in a wolframite can be attributed to the charge imbalance between the Fe^{3+} and Nb^{5+} cation, and thus the addition of TiO_2 on both layer decreases the charge imbalance amongst the cation planes and the cation ordering[50]. Tena et al.[51] and Balzer et al.[44] studied the phase transition of $FeNbO_4$-TiO_2 solid solution and found similar results. With regard to the sample with an x value of

0.25, the slowly cooled sample preserved the rutile structure where the randomly distributed cations are in linear interstice of *hcp* oxide ions[52], indicating that the addition of Ti^{4+} cation can preserve the high temperature phase of $FeNbO_4$-based materials by decreasing the bond length/charge length difference of cations between the layers[53].

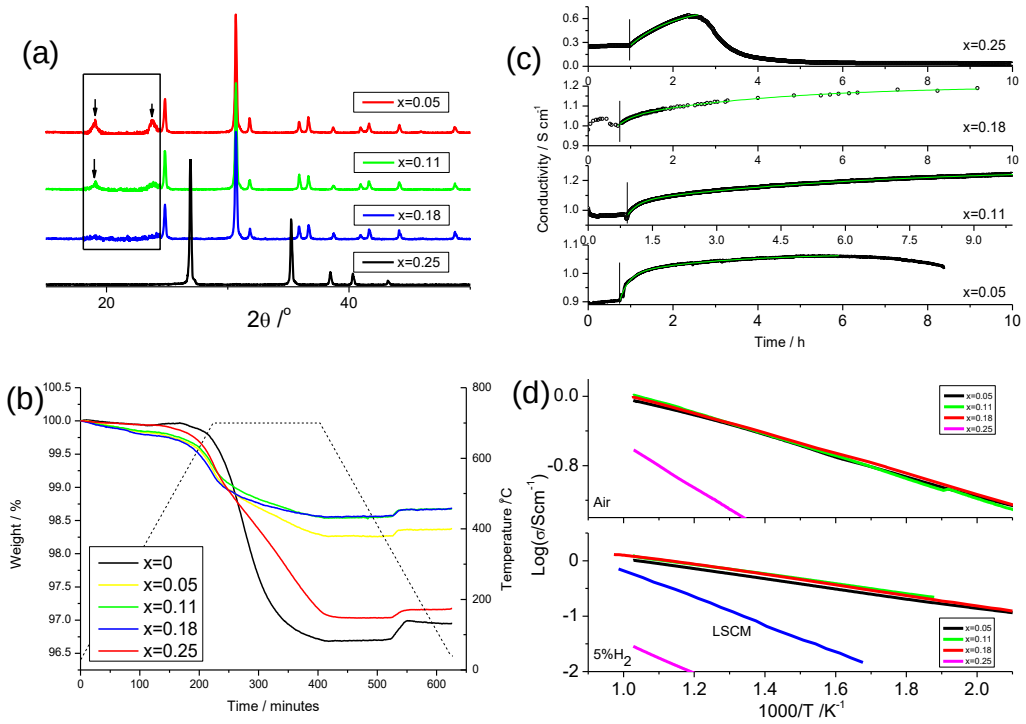

Figure 4 (a) XRDs and (b)the corresponding TGA curves of $Ti_{2x}(Fe_{0.985}Nb_{1.015})_{1-x}O_4$ ($0.05 \leqslant x \leqslant 0.25$) (the data in the rectangle box is magnified by 5 times to highlight the peak for the monoclinic phase); (c) Conductivity variation of the $Ti_{2x}(Fe_{0.985}Nb_{1.015})_{1-x}O_4$ ($0.05 \leqslant x \leqslant 0.25$) samples at 700 °C and (d) Arrhenius plots of conductivity during the heating in air and cooling in 5% H_2. The rectangle in (a) shows the location of peaks due to the monoclinic polymorphs. The vertical lines in (c) delimit the initiation of reduction process and the blue line in (d) is the conductivity of $La_{0.75}Sr_{0.25}Cr_{0.5}Mn_{0.5}O_3$ (LSCM) in 5% H_2.

The addition of Ti^{4+} cations in the structure decreases the weight loss at 700 °C, which can be seen in the TGA curves (Figure 4b), except for the one with a rutile structure when

x reaches 0.25. The weight loss can be affected by several factors: (1) the cation ordering/disordering in the structure that might affect the oxygen vacancies; (2) the incorporation of stable Ti^{4+} requiring a high-temperature reduction; (3) the shortening of bond length (Fe-O) that might have caused by the addition of Ti^{4+}cation with smaller ionic radii. It should be noted that the sample most heavily doped by TiO_2 (x=0.25) showed much higher oxygen loss than the its peers, indicating that the random zig-zag distribution of cations in an α-PbO_2 structure are beneficial to the structure stability under a reducing atmosphere. The XRDs of the $Ti_{2x}(Fe_{0.985}Nb_{1.015})_{1-x}O_4$ ($0.1 \leqslant x \leqslant 0.25$) samples (Figure S1) after the TGA measurement indicate that the samples maintain the α-PbO_2 structure if x is less than 0.18. Specifically, TFN-36 maintains the original structure after the reduction under 5% H_2, but there is a peak shift to the low-angle side owing to the formation of Fe^{2+} cation along with the oxygen loss causing the chemical expansion[33].

The addition of TiO_2 affects not only the crystal structure and oxygen loss under a reducing atmosphere, but also the conductivity of the materials (Figure 4c, d). For the TiO_2-doped samples, the conductivity in air or 5 % H_2 changed very little with the incorporation of the relatively stable Ti^{4+} cation providing x is not greater than 0.18, but the conductivity of the rutile one with x=0.25 is much smaller. The samples with moderate TiO_2 doping (x=0.11 and 0.18) show superior stability at reducing atmosphere (700 °C, 5% H_2). The conductivity of the doped samples (x=0.05, 0.11 and 0.18) is higher than the *p*-type semiconductor LSCM[13] under the same situation at 700 °C and the advantage is more obvious at lower temperature due to the smaller activation energy[54].

Fuel cell fabrication and electrochemical performance

According the above study, the $Ti_{0.36}(Fe_{0.985}Nb_{1.015})_{0.84}O_4$ or TFN-36, maintains the α-PbO_2 structure even under a normal cooling and is thermally stable up to a temperature of 700 °C. This material thus can be selected to construct the oxide anode. The compatibility of TFN-36 with GDC electrolyte was studied using XRDs (Figure 5) of the mixture calcined at 1000 °C for 4 hours. There could be some variation in the peaks for the wolframite

phase during the calcination, but there is no reaction between GDC and TFN-36.

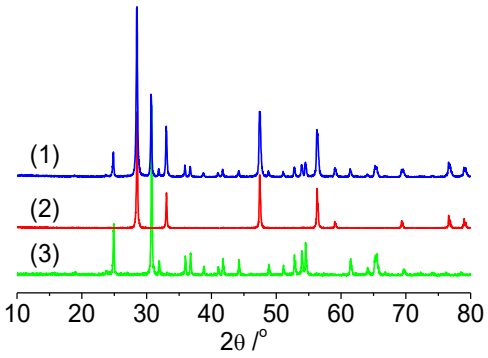

Figure 5 XRD of the admixture of TFN-36 and GDC (line 1) after calcination at 1000 °C for 4 hours. The XRDs of TFN-36 (line 3) and GDC (line 2) were provided for comparison.

X-ray photoelectron spectroscopy (XPS, Figure 6) was performed on the TFN-36 sample calcined in air followed by reduction in 5% H_2. The high-resolution Fe2p spectrum showed two split spin-orbit components and the $Fe2p_{3/2}$ peak for the sample prepared in air can be de-convoluted to a doublet peaked with binding energies of 710.9 and 712.8 eV, which could be assigned to Fe^{2+} and Fe^{3+}[33] respectively. The $[Fe^{2+}]/[Fe^{2+}+Fe^{3+}]$ is calculated to be 0.5, which depends on the oxygen vacancies. For the samples reduced under 5% H_2, the intense peak at 710.85 eV for Fe^{2+} dominates over the peak for Fe^{3+} that merges with the plasmonic peak. Combining the spectral calculations with $i_{0.36}(Fe_{0.985}Nb_{1.015})_{0.84}O_{3.68}$ containing high oxygen vacancies to confirm that no metal iron was formed. In addition, the decrease of the plasmonic peak at 720 eV is also an indication of the reduction of Fe^{3+} cation to Fe^{2+}. The core-level spectra for $Ti2p_{3/2}$ and Nb3s show singlets peaking at 458.3 and 470.5 eV, respectively, and remain constant before and after the reduction, suggesting Nb^{5+} and Ti^{4+} are not subjected to valence change under a reduction at 700 °C.

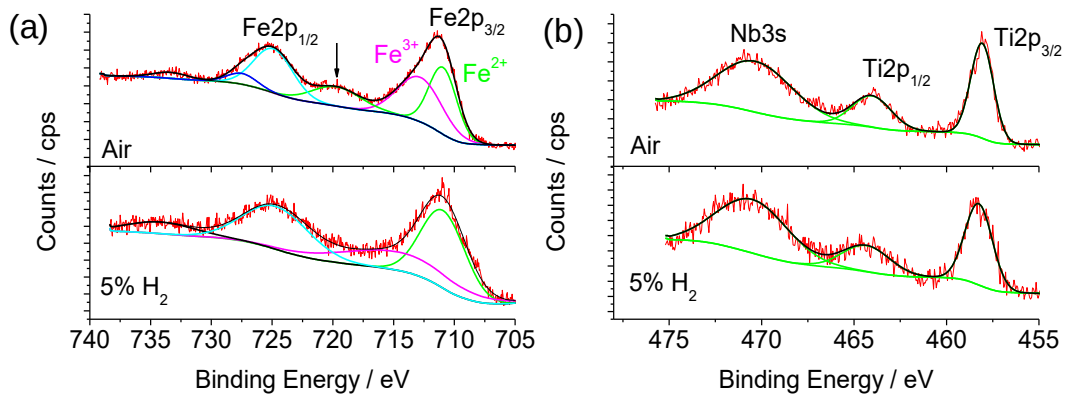

Figure 6. XPS spectra in terms of Fe2p (a) and Nb1s and Ti2p (b) in air and after the reduction in 5% H_2. The arrow in (a) indicates the plasmonic peak.

The cell performance of the TFN-36|GDC (200 μm)|LSCF/GDC cell using air and humidified H_2 (3% H_2O) as the respective oxidant and fuel is shown in Figure 7a. The OCV of the cell (0.77 V at 700 °C and 0.81 V at 600 °C) is lower than the theoretical values given by Nernst equation (above 1.0 V at both temperatures). The difference is possibly associated with electronic conduction of GDC electrolyte due to the reduction of Ce^{4+} to Ce^{3+}[1, 55]. The I-V and I-P curves indicate a maximum power of 122 mW cm^{-2} and 180 mW cm^{-2} at 700 °C for the cell anode without and with 0.5% catalyst, respectively (Figure 7b). Compared to the $FeNbO_4$|GDC (200 μm)|LSCF/GDC cell, the doping of TiO_2 to the cell anode enhanced the maximum power density by a factor of 3.9, from 25 mW cm^{-2} to 122 mW cm^{-2} (Figure S2a). The electrochemical impedance plots (Figure 7c) indicate that the polarization resistance calculated from the span of the impedance spectra on x-axis for the cell without and with Pd catalyst are 0.36 Ωcm^2 and 0.13 Ωcm^2 at 700 °C, respectively. However, the polarization resistance of the cell is 2.4 Ωcm^2 at 700 °C (Figure S2b), the doping of TiO_2 to the cell can improve the electrochemical performance of the cell and this could be related to better electric (ionic and/or electronic) conductivity. This polarization resistance of the LSCF/GDC composite cathode is 0.1 Ωcm^2 at 700 °C (Figure S3) and the polarization resistance of the TFN-36 anode should be 0.26 Ωcm^2 and 0.03 Ωcm^2 for the cell without and with Pd. Specifically, the polarization resistance at 600 °C

with Pd is 0.89 Ωcm^2, which is larger than Pd and GDC co-infiltrated $Sr_{0.94}Ti_{0.9}Nb_{0.1}O_3$ backbone (0.6 Ωcm^2 at 600 °C)[56] or Pd-GDC infiltrated $Y_{0.7}Ca_{0.3}Cr_{1-x}Cu_xO_{3-\delta}$ anode (0.013 Ωcm^2)[54]. The oxidation of H_2 on the anode of an SOFC depends on the triple-phase boundary (TPB) length, tortuosity of gas path and the electronic, ionic transport path[57]. The extension of reaction sites is usually reported to be efficient if ionic oxides and metal catalyst (such as Ni, Pt and Pd) are impregnated sequentially[11, 12, 26, 54], and thus the polarization resistance determined from the cell with Pd impregnation alone indicates that the ionic conductivity of TFN-36 under the fuel condition is inferior to the GDC.

After the fuel was switched to LPG, the OCV of the cell decreased to 0.68 V and a peak power of 69 mW cm^2 can be obtained after 0.5 hour of equilibration (Figure 7d). The decrease in peak power can be explained by the increase in the polarization resistance from 0.36 Ωcm^2 to 0.71 Ωcm^2 when LPG replaced H_2 as the fuel (Figure S4), accompanied by decrease in OCV. The stability of the cell with TFN-36 was investigated under LPG fuel at a bias of 0.5 V and one can see that the cell suffers from degradation over the initial 26 hours, the power of cell decreased from 65 mW cm^{-2} to 36 mW cm^{-2} (Figure S5). For an anode with *n*-type titanate perovskite, similar degradation was found under a H_2 fuel and this could be related to the oxidation of anode under bias that causing the decrease in oxygen vacancy and microstructure variation[12]. Nonetheless, with LPG as fuel, the degradation can also come from the carbon deposition or sulfide that inhibits the diffusion of fuel to the anode/electrolyte interface[14, 58]. However, the oxide-anode lasted much longer than a Ni-cermet based anode as the latter can be utterly dysfunctional in the first half an hour as a result of carbon deposition [59].

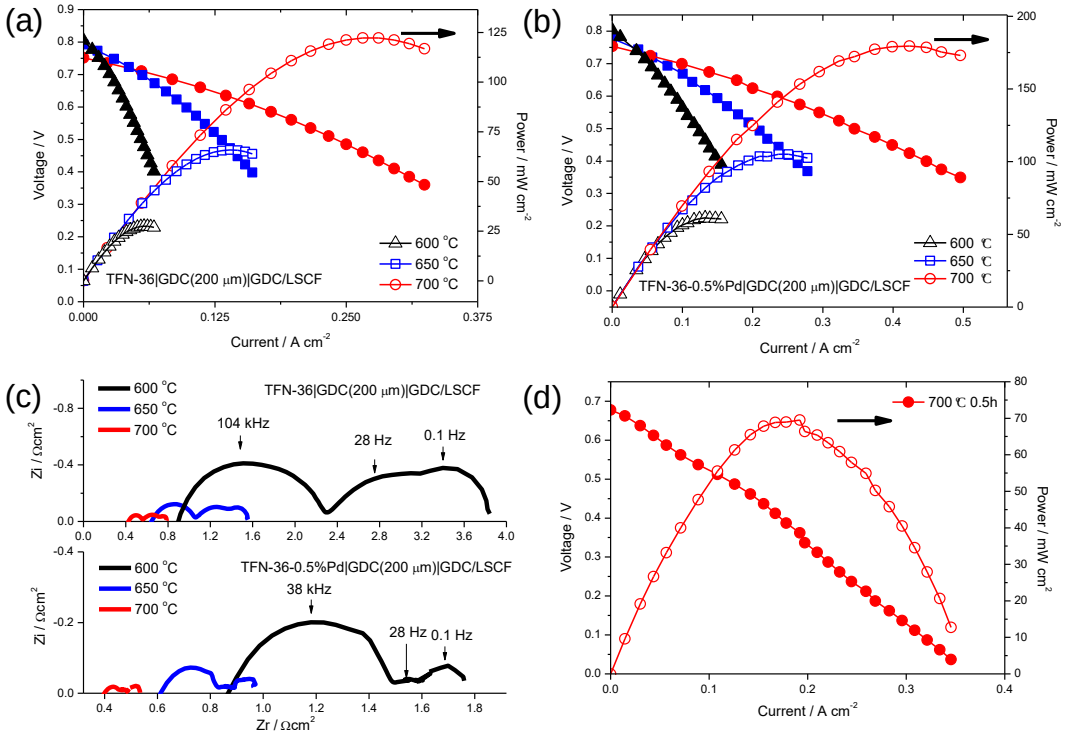

Figure 7 I-V and I-P curve of the cell without (a) and with Pd catalyst (b) on the anode at 600 °C, 650 °C and 700 °C and the corresponding Nyquist plots of electrochemical impedance spectra (c) at OCV. (d) I-V and I-P curve of the cell at 700 °C with TFN-36 anode under LPG fuel at 0.5 hour.

Post-test microstructure of the anode

Figure 8 shows the SEM images of the sample after the test under H_2 and LPG fuel. The painted anode is around 56 μm in thickness in the cross section image (Figure 8a) and is highly porous, which could be beneficial for the gas transport to the electrode/electrolyte interface. A good bonding between the electrode and electrolyte is observed and the grain size of the oxide anode is around 1 μm (Figure 8b). The enlarged TFN-36 anode after operation with LPG for five hours (Figure 8c) did show some needle-like particles around 100 nm in width which could be related to the deposition of carbon on the surface. However, it should be noted that after the test under LPG, the alumina tube was coated with a thick layer of carbon due to the thermal decomposition of the fuel, but the survival of the cell after 24 hours could be related to the superior coke resistance of the electrode

under a bias at 0.5 V.

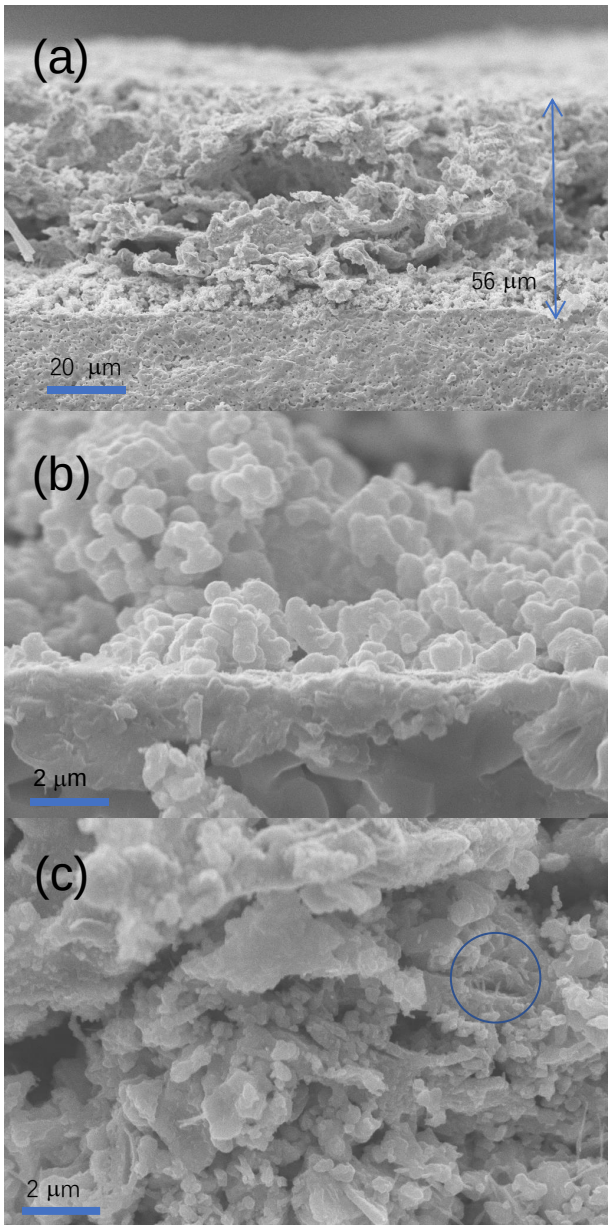

Figure 8 (a) SEM image of the cross section of the TFN-36 anode on GDC electrolyte after the testing at 700 °C. Enlarged SEM images of the sample tested under humidified H_2 (b) and LPG (c). The circle in (c) highlights the needle-shape nanoparticles on the oxide surface.

Conclusions

Wolframite-type $Fe_{1-\gamma/3}Nb_{1+\gamma/3}O_4$ ($0 \leqslant \gamma \leqslant 0.60$) has been synthesized at 1250 °C as a solid solution between $FeNbO_4$-$FeNb_2O_6$. The α-PbO_2 type $FeNbO_4$ with cation disordering would be beneficial to the structure stability under hydrogen and high electric conductivity (above 2 S cm^{-1}) in both air and reducing conditions. The doping of Ti^{4+} on Fe^{3+} and Nb^{5+} sites stabilizes the α-PbO_2 structure by alleviating the charge difference tween the cation layers. TFN-36 ($Ti_{0.36}(Fe_{0.98}5Nb_{1.015})_{0.84}O_{4-\delta}$) contains an oxygen non-stoichiometry, δ, of 0.32 after the reduction process, which could give high oxide-ion conduction. The cell without and with Pd infiltrated TFN-36 anode showed a maximum power density of 122 mW cm^2 and 180 mW cm^2 at 700 °C for an electrolyte support cell, respectively. The cell with TFN-36 anode showed a degradation (20% during the 5 to 26 hours aging) under an LPG fuel and the deposition of carbon had limited effect on the porosity and gas transport in the anode. As the $FeNbO_4$ oxide can tolerate the $Fe^{3+/2+}$ deficiency, the exsolution of metal catalyst on the surface under reducing condition is under investigation to improve the performance and stability of the anode under hydrogen or carbonaceous fuels.

Acknowledgement

We would like to acknowledge the support from the Natural Science Foundation of China (NSFC, 51702264, 41371275), National Key Research and Development Program of China (grant No. 2018FYD0200701). C.N. also thank the Award of Bayu Young Scholarship from the Chongqing Teaching Committee.

References

[1] N.Q. Minh, *J. Am. Ceram. Soc.* **76** (1993) (3) 563.

[2] A. Atkinson, S. Barnett, R.J. Gorte, J.T.S. Irvine, A.J. McEvoy, M. Mogensen, S.C. Singhal, J. Vohs, *Nat. Mater.* **3** (2004) (1) 17.

[3] T. Hibino, A. Hashimoto, T. Inoue, J. Tokuno, S. Yoshida, M. Sano, *Science* **288** (2000) (5473) 2031.

[4] E.P. Murray, T. Tsai, S.A. Barnett, *Nature* **400** (1999) (6745) 649.

[5] Y. Zhang, F. Yu, X. Wang, Q. Zhou, J. Liu, M. Liu, *J. Power Sources* **366** (2017) 56.

[6] F.J. Garcia-Garcia, F. Yubero, A.R. González-Elipe, R.M. Lambert, *Int. J. Hydrogen Energy* **43** (2018) (2) 885.

[7] J.G. Lee, J.H. Park, Y.G. Shul, *Nat. Commun.* **5** (2014) 4045.

[8] Z. Shao, S.M. Haile, *Nature* **431** (2004) (7005) 170.

[9] W. Wang, C. Su, Y. Wu, R. Ran, Z. Shao, *Chem Rev* **113** (2013) (10) 8104.

[10] G. Corre, G. Kim, M. Cassidy, J.M. Vohs, R.J. Gorte, J.T.S. Irvine, *Chem. Mater.* **21** (2009) (6) 1077.

[11] L. Lu, C. Ni, M. Cassidy, J.T.S. Irvine, *J. Mater. Chem. A* **4** (2016) 11708.

[12] C. Ni, L. Lu, D.N. Miller, M. Cassidy, J.T.S. Irvine, *J. Mater. Chem. A* **6** (2018) (13) 5398.

[13] S. Tao, J.T.S. Irvine, *Nat. Mater.* **2** (2003) (5) 320.

[14] Y.H. Huang, R.I. Dass, Z.L. Xing, J.B. Goodenough, *Science* **312** (2006) (5771) 254.

[15] M.-J. Lee, J.-H. Shin, M.-J. Ji, H.-J. Hwang, *J. Power Sources* **374** (2018) 181.

[16] S. Sengodan, Y.-W. Ju, O. Kwon, A. Jun, H.Y. Jeong, T. Ishihara, J. Shin, G. Kim, *ACS Sustainable Chemistry & Engineering* **5** (2017) (10) 9207.

[17] Y. Li, X. Chen, Y. Yang, Y. Jiang, C. Xia, *ACS Sustainable Chemistry & Engineering* **5** (2017) (12) 11403.

[18] T. Wei, Y. Ji, X. Meng, Y. Zhang, *Electrochem. Commun.* **10** (2008) (9) 1369.

[19] J. Feng, J. Qiao, W. Wang, Z. Wang, W. Sun, K. Sun, *Electrochim. Acta* **215** (2016) 592.

[20] B.H. Park, G.M. Choi, *Electrochim. Acta* **182** (2015) 39.

[21] A.D. Aljaberi, J.T.S. Irvine, *J. Mater. Chem. A* **1** (2013) (19) 5868.

[22] A. Gondolini, E. Mercadelli, G. Constantin, L. Dessemond, V. Yurkiv, R. Costa, A. Sanson, *J. Eur. Ceram. Soc.* **38** (2018) (1) 153.

[23] D. Marrocchelli, S.R. Bishop, H.L. Tuller, B. Yildiz, *Adv. Funct. Mater.* **22** (2012) (9) 1958.

[24] K.H. Ng, H.A. Rahman, M.R. Somalu, *Int. J. Hydrogen Energy* (2018).

[25] K.-J. Pan, A.M. Hussain, E.D. Wachsman, *J. Power Sources* **347** (2017) 277.

[26] C.S. Ni, J. Vohs, R.J. Gorte, J.T.S. Irvine, *J. Mater. Chem. A* **2** (2014) 19150.

[27] J.T.S. Irvine, D. Neagu, M.C. Verbraeken, C. Chatzichristodoulou, C. Graves, M.B. Mogensen,

Nature Energy **1** (2016) 15014.

[28] C. Ni, Q. Zeng, D. He, L. Peng, D. Xie, J.T.S. Irvine, S. Duan, J. Ni, *J. Mater. Chem. A* **7** (2019) 26944.

[29] D. Neagu, G. Tsekouras, D.N. Miller, H. Ménard, J.T.S. Irvine, *Nature Chem.* **5** (2013) 916.

[30] Z. Jiang, C. Xia, F. Chen, *Electrochim. Acta* **55** (2010) (11) 3595.

[31] X. Chen, W. Ni, J. Wang, Q. Zhong, M. Han, T. Zhu, *Electrochim. Acta* **277** (2018) 226.

[32] X.B. Zhu, Z. Lu, B. Wei, M.L. Liu, X.Q. Huang, W.H. Su, *Electrochim. Acta* **55** (2010) (12) 3932.

[33] C. Ni, J. Feng, J. Cui, J. Zhou, J. Ni, *J. Electrochem. Soc.* **164** (2017) (4) F283.

[34] R. Theissmann, H. Ehrenberg, H. Weitzel, H. Fuess, *Solid State Sci.* **7** (2005) (6) 791.

[35] S. Ananta, R. Brydson, N.W. Thomas, *J. Eur. Ceram. Soc.* **19** (1999) (4) 489.

[36] H. Wei, K. Xie, J. Zhang, Y. Zhang, Y. Wang, Y. Qin, J. Cui, J. Yan, Y. Wu, *Sci. Rep.* **4** (2014) 5156.

[37] R. Haugsrud, T. Norby, *Nat. Mater.* **5** (2006) (3) 193.

[38] S. Kanti Biswas, T. Gnanasekaran, T. Kumar Ghorai, P. Pramanik, *J. Electrochem. Soc.* **155** (2008) (1) J26.

[39] C. Ni, G. Hedley, J. Payne, V. Svrcek, C. McDonald, L.K. Jagadamma, P. Edwards, R. Martin, G. Jain, D. Carolan, D. Mariotti, P. Maguire, I. Samuel, J. Irvine, *Nat. Commun.* **8** (2017) (1) 170.

[40] M. Lv, S. Ni, Z. Wang, T. Cao, X. Xu, *Int. J. Hydrogen Energy* **41** (2016) (3) 1550.

[41] E. Schmidbauer, J. Schneider, *J. Solid State Chem.* **134** (1997) (2) 253.

[42] C. Ni, M. Cassidy, J.T.S. Irvine, *J. Eur. Ceram. Soc.* **38** (2018) (16) 5463.

[43] X. Huang, J. Feng, H.R.S. Abdellatif, J. Zou, G. Zhang, C. Ni, *Int. J. Hydrogen Energy* **43** (2018) (18) 8962.

[44] B. Balzer, H. Langbein, *Cryst. Res. Technol.* **31** (1996) (1) 93.

[45] K. Brandt, *Arkiv. Kemi. Mineralog.* **A17** (1943) 1.

[46] A. Lashtabeg, J. Canales-Vazquez, J.T.S. Irvine, J.L. Bradley, *Chem. Mater.* **21** (2009) (15) 3549.

[47] H. Taguchi, M. Sonoda, M. Nagao, *J. Solid State Chem.* **137** (1998) (1) 82.

[48] C.S. Ni, J.P. Ni, Z.Z. Zhou, M. Jin, *J. Alloys Compd.* **709** (2017) 789.

[49] M.L. Blanco, SÍNTESIS, CARACTERIZACIÓN ESTRUCTURAL Y ELÉCTRICA DE MATERIALES TIPO COLUMBITA Y TRI-RUTILOS ANb2-xTaxO6(A=Ni y Mn) Y DE ALGUNOS DERIVADOS

SUSTITUIDOS-Ti UNIVERSIDAD CARLOS III DE MADRID (2011), p.370.

[50] Z. Pan, X. Yu, Q. Wang, J. Cao, F. Pan, C. Liang, F. Lu, X. Kuang, C. Su, J. Wang, L. Fang, *J. Mater. Chem. C* **2** (2014) (25) 4957.

[51] M.A. Tena, P. Escribano, G. Monrós, J. Carda, J. Alarcón, *Mater. Res. Bull.* **27** (1992) (11) 1301.

[52] S.-L. Hwang, P. Shen, H.-T. Chu, T.-F. Yui, *Science* **288** (2000) (5464) 321.

[53] A. Baumgarte, R. Blachnik, *J. Alloys Compd.* **215** (1994) (1) 117.

[54] A.M. Hussain, K.-J. Pan, Y.-L. Huang, I.A. Robinson, C. Gore, E.D. Wachsman, *ACS Appl. Mater. Interfaces* **10** (2018) (42) 36075.

[55] E.D. Wachsman, K.T. Lee, *Science* **334** (2011) (6058) 935.

[56] A.M. Hussain, J.V.T. Høgh, W. Zhang, N. Bonanos, *J. Power Sources* **216** (2012) 308.

[57] J.R. Wilson, W. Kobsiriphat, R. Mendoza, H.-Y. Chen, J.M. Hiller, D.J. Miller, K. Thornton, P.W. Voorhees, S.B. Adler, S.A. Barnett, *Nat. Mater.* **5** (2006) (7) 541.

[58] B. Stoeckl, V. Subotić, D. Reichholf, H. Schroettner, C. Hochenauer, *Electrochim. Acta* **256** (2017) 325.

[59] L. Yang, Y. Choi, W. Qin, H. Chen, K. Blinn, M. Liu, P. Liu, J. Bai, T.A. Tyson, M. Liu, *Nat. Commun.* **2** (2011) 357.